

# The evolution of planetary nebulae

## II. Circumstellar environment and expansion properties<sup>\*,\*\*</sup>

D. Schönberner<sup>1</sup>, R. Jacob<sup>1</sup>, M. Steffen<sup>1</sup>, M. Perinotto<sup>2</sup>, R. L. M. Corradi<sup>3</sup>, and A. Acker<sup>4</sup>

<sup>1</sup> Astrophysikalisches Institut Potsdam, An der Sternwarte 16, 14482 Potsdam, Germany  
e-mail: [deschoenberner;msteffen]@aip.de

<sup>2</sup> Dipartimento di Astronomia e Scienza dello Spazio, Largo E. Fermi 2, 50125 Firenze, Italy  
e-mail: mariop@arcetri.astro.it

<sup>3</sup> Isaac Newton Group of Telescopes, Ap. de Correos 321, 38700 Santa Cruz de la Palma, Canary Islands, Spain  
e-mail: rcorradi@ing.iac.es

<sup>4</sup> Observatoire Astronomique, 11 rue de l'Université, 67000 Strasbourg, France  
e-mail: acker@astro.u-strasbg.fr

Received 15 July 2004 / Accepted 15 October 2004

**Abstract.** We investigate and discuss the expansion properties of planetary nebulae by means of 1D radiation-hydrodynamics models computed for different initial envelope configurations and central star evolutionary tracks. In particular, we study how the expansion depends on the initial density gradient of the circumstellar envelope and show that it is possible to derive information on the very last mass-loss episodes during the star's final evolution along and off the asymptotic giant branch. To facilitate the comparison of the models with real objects, we have also computed observable quantities like surface brightness and emission-line profiles.

With the help of newly acquired high-resolution emission-line profiles for a sample of planetary nebulae we show that models with initial envelopes based on the assumption of a stationary wind outflow fail to explain the observed expansion speeds of virtually all of the observed planetary nebulae. Instead it must be assumed that during the very last phase of evolution along the final asymptotic giant branch evolution the mass-loss rate increases in strength, resulting in a much steeper slope of the circumstellar radial density distribution. Under these conditions, the expansion properties of the nebular gas differ considerably from the self-similar solutions found for isothermal conditions.

Furthermore, the mass loss must remain at a rather high level until the stellar remnant begins to evolve quickly towards the central star regime. Current theoretical computations of dust-driven mass-loss which are restricted to rather low temperatures cannot be applied during the star's departure from the asymptotic giant branch.

**Key words.** hydrodynamics – radiative transfer – ISM: planetary nebulae: general – stars: AGB and post-AGB

### 1. Introduction

The severe mass-loss which low and intermediate mass stars suffer during their final evolution along the asymptotic giant branch (AGB) is still an important but unsolved issue from the theoretical as well as from the observational point of view. Next to supernova explosions, these stars provide important contributions to the recycling of matter in galaxies by means of

their dense winds which are self-polluted by nucleosynthesis products dredged-up from the stellar interiors. The lifetimes of high mass-loss phases are short and thus difficult to observe, although these phases are the most important ones for the enrichment of the interstellar medium and determine the fraction of a star's initial mass that remains locked for ever as a white dwarf (initial final mass relation, Weidemann 2000).

Observationally, it appears now well established that the mass-loss rates of AGB stars increase rapidly with luminosity (e.g. Alard et al. 2001). Theoretical calculations of the mass loss as a function of the stellar parameters are available for carbon-rich surface compositions (cf. Wachter et al. 2002), but the results are conflicting: recent calculations of Sandin & Höfner (2003) predict much lower mass-loss rates. Nevertheless, the existing mass-loss prescriptions, if coupled

\* Based on observations obtained at the 3.5 m NTT and the 1.2 m CAT telescope of the European Southern Observatory, La Silla, and at the 2.6 m NOT telescope operated on the island of La Palma by NOTSA, in the Spanish Observatorio del Roque de Los Muchachos of the Instituto de Astrofísica de Canarias.

\*\* Dedicated to Prof. V. Weidemann on the occasion of his 80th birthday, October 3, 2004.

to evolutionary calculations, predict also an increase of the mass loss towards the tip of the AGB. These dust-driven winds are, however, very sensitive to the stellar effective temperature. They are not suited to predict how the mass loss behaves when  $T_{\text{eff}}$  increases as the remnant star moves slowly off the tip of the AGB, but if applied formally, they predict a strong mass-loss decrease when the AGB remnant becomes hotter.

The mass loss occurring during the transition of a remnant from the AGB towards the central star regime is unimportant for the star's total mass budget, but of utmost importance for the evolutionary time scales (Schönberner 1990). Only if the mass-loss rate exceeds the burning rate by orders-of-magnitude until rather large effective temperatures between 5000 and 6000 K are reached, the evolution is fast enough so as to be in agreement with the existence of post-AGB stars with strong dust-shell emission (cf. Hrivnak et al. 1989). All stellar evolution modelers have to resort to rather ambiguous assumptions about the mass loss that can only be justified post-facto if the results comply with the observational evidences.

There exist a large sample of objects that must contain direct and/or indirect information about the very last mass-loss episodes discussed above: the planetary nebulae (PNe). Their central stars are the immediate successors of AGB stars and on the transit to become white dwarfs. The former AGB wind is reshaped by both the photo-ionization due to the strong UV radiation field of the central star and the dynamical impact of the fast but tenuous central-star wind when it collides with the much slower AGB material (cf. Marten & Schönberner 1991; Mellema 1994; Schönberner & Steffen 1999). The PN proper contains thus only indirect clues concerning AGB mass-loss properties. The only direct information about the preceding mass-loss is provided by the dynamically little affected haloes of PNe (Corradi et al. 2003a). Given the low surface brightness of the haloes, very little is known about their physical properties, and for the time being one has to resort to the much brighter PNe proper in order to retrieve the hidden information about the mass-loss behaviour while a star leaves the AGB.

Progress in our understanding of how shapes and expansion properties of planetary nebulae depend on the circumstellar environment set up during the last phases of evolution along the AGB demands detailed numerical studies by means of an accurate radiation-hydrodynamics code. Such a study has recently been published by Perinotto et al. (2004, henceforth Paper I), and the main conclusions are:

- Provided that there is a mass-loss rate at the end of the AGB of at least  $1 \times 10^{-5} M_{\odot} \text{ yr}^{-1}$ , the expanding ionization front is of type D, i.e. it is led by a shock which expands supersonically into the ambient neutral and cool AGB wind. This shock and the high thermal pressure of the ionized matter completely redistribute density and velocity structures set up earlier.
- After the AGB wind becomes fully ionized, a double shell structure develops, consisting of the *shell* which is the remnant of the shock wave set up earlier by the D-type ionization front, and the *rim*, created from compressed shell matter by the dynamical interaction with the central-star wind. The shell's shock front determines now the size of

the PN, and its speed gives the expansion rate which is, in principle, not measurable by spectroscopic means. Flow velocities measured by the Doppler splitting of emission lines should not be mistaken for this expansion since they are matter velocities belonging to regions well behind the shock, and which are always below the shock speed.

- The shell shock expansion relative to the ambient AGB wind is controlled by the actual sound speed and the density gradient of the AGB wind. It is found that for models with stationary AGB winds, the flow is not accelerated sufficiently by the shock as to explain the measured Doppler-splits of the shell's signature in the emission lines. A steeper density gradient of the AGB wind is necessary to explain the observed flow speeds in the shell, and also the radial run of its surface brightness. The conclusion is that mass-loss rates should increase considerably towards the end of the AGB evolution, and that the high rate must continue until the remnant leaves rapidly the tip of the AGB.
- The rim is physically a bubble blown by the central-star wind into the expanding shell matter and is confined by a contact discontinuity and a leading shock. It develops rapidly into the brightest part of a typical round/elliptical planetary nebula. The overall expansion property of the rim matter is controlled by the balance between the thermal pressure of the shocked stellar wind and the ambient shell matter and depends thus very much on the wind strength itself and its development with time. The rim's leading shock is at first very weak, but becomes stronger and faster in the course of the evolution, and the rim may finally overtake the shell.

From the theoretical side, the expansion of planetary nebulae is practically described by the evolution of an H II region into an environment with a power-law density distribution,  $\rho \propto r^{-\alpha}$ , as investigated by Franco et al. (1990), and more recently by Shu et al. (2002). In this context it has been shown that there exists a critical value of the density power law index,  $\alpha_{\text{crit}} = 1.5$ , below which the ionization front always remains trapped behind the shock front. For  $\alpha > 1.5$ , the ionization front will eventually overtake its shock, and the latter will expand supersonically into its now ionized surroundings. This is the so-called “champagne phase” of expansion.

By means of approximate solutions of such “champagne” flows with power-law density distributions Franco et al. (1990) showed that the shock speed increases with the power law index  $\alpha$ , and that one has to distinguish between two regimes: For  $\alpha < 3$ , the shock front is weak and accelerates slowly with  $\alpha$ , and the evolution is almost isothermal. For  $\alpha \geq 3$ , the shock becomes stronger, more adiabatic, and depends more strongly on  $\alpha$ , and its expansion speed increases with time. Shu et al. (2002) computed self-similar solutions for strictly isothermal champagne flows with  $1.5 \leq \alpha < 3$ . Because of the isothermal assumption, the shock-front velocity becomes infinite for the self-similar solution with  $\alpha = 3$ .

There are, however, two important differences between planetary nebulae and H II regions: the matter of the former is initially not at rest, and the fast evolution of the central star leads to a concomitant variation of the ionizing radiation field.

Since  $\alpha$  is usually expected to be close to or even larger than 2, the flow of the PN material will always enter the champagne phase, to be identified with the optically thin stage. Only in the exceptional case of a very rapidly dimming central star this phase will be missed (see discussion in Paper I).

The dependence of the expansion speed of thermally-driven shock waves on the density gradient of the circumstellar matter opens the possibility to determine this slope and hence the time variation of the very last mass-loss episodes. It is thus the aim of this paper to investigate in more detail the kinematics of PNe by modelling their evolution numerically by means of simple initial models where the effect of any parameter variation can easily be studied and assessed.

We begin in Sect. 2 with a description and discussion of the properties of our radiation-hydrodynamics models and continue in Sect. 3 with a detailed discussion of how planetary nebulae expansion depends on the density distribution of the ambient medium. In Sect. 4 we compare theory with new observations and discuss the final conclusions in Sect. 5. Part of this study has already been presented in a different context by Schönberner et al. (2004).

## 2. The hydrodynamical models and their analysis

The basis of the present study is provided by the set of spherical radiation-hydrodynamics models described extensively in Paper I, which the reader is referred to concerning all the details of computing and modelling. We used for our purpose the TYPE A sequences listed in Table 1 of Paper I, i.e. those which correspond to initial configurations with  $\alpha = 2$  and constant wind velocity.

We computed an additional TYPE A sequence with a new post-AGB track for a mass of  $0.595 M_{\odot}$ , gained by interpolating between the  $0.605$  and  $0.565 M_{\odot}$  tracks of Paper I. This model evolves more slowly than the  $0.605 M_{\odot}$  model: it needs about 10 000 yrs to reach the turn-around point instead of 7000 yrs. The new model provides a longer time span before the star fades and the recombination epoch begins and appears thus to be more appropriate for representing planetary nebulae. The overall evolutionary properties of this post-AGB model are depicted in Fig. 1.

The models with  $\alpha = 2$  initial envelopes were then supplemented by a family of models with power-law density distribution where  $\alpha$  ranges from 1.75 till 3.5 in steps of 0.25. The inner boundary is set at  $r = 4 \times 10^{14}$  cm, the outer boundary at  $r = 2.8 \times 10^{18}$  cm. All these models are normalized in such a way that at  $r = 3 \times 10^{16}$  cm the density is  $n = 10^5 \text{ cm}^{-3}$ , corresponding to a mass-loss rate of  $4.3 \times 10^{-5} M_{\odot} \text{ yr}^{-1}$ . The initial velocity of the AGB wind was set to  $10 \text{ km s}^{-1}$  in all cases. For  $\alpha = 3$  an additional model with  $V_{\text{agb}} = 20 \text{ km s}^{-1}$  was also computed. The elemental composition was chosen identical to the one used earlier and is typical for Galactic disk planetaries (Table 1).

Our new power-law envelope configurations were coupled to the  $0.595 M_{\odot}$  post-AGB model shown in Fig. 1 such that starting at age zero the wind of the central star was used as input at the inner boundary of the grid. The full radiation-hydrodynamics evolution was followed for about 10 000 years until

**Table 1.** Elemental abundances used for the computation of our hydrodynamical models, in (logarithmic) number fractions relative to hydrogen = 12.

H	He	C	N	O	Ne
12.00	11.04	8.89	8.39	8.65	8.01

recombination sets in beyond the turn-around point. The structure variables of the model nebulae served then as input for several supplementary codes by which important observable quantities can be computed: emission-line luminosities and surface brightnesses, and detailed line profiles along different line-of-sights with different spatial resolutions, up to the case where the whole object is embraced by the numerical aperture. The code for the computation of the emission-line profiles is an updated version of the one originally used by Gesicki et al. (1996), made available to us by the authors. We emphasize that these codes for the computation of observable quantities like surface brightness distribution and line profiles are indispensable tools which allow a direct comparison of our models with real objects.

Additional IDL routines were developed with the goal to extract automatically the positions of shock fronts from the computed model structures and to determine the flow variables before and behind these shocks. Furthermore, we fitted the computed line profiles by multi-component Gaussians (usually four) in order to determine the bulk motions within the individual nebular shells. Although the individual contributions of the shells are not necessarily of Gaussian shapes, the determination of typical velocities by decomposition into Gaussians worked very well. With these supplementary diagnostic tools at hand we are able to investigate the kinematical structure of our hydrodynamic models in a more sophisticated manner than before.

Our method is illustrated in Fig. 2 which shows a typical model structure (density and velocity), the corresponding surface brightness in  $H\alpha$ , and the emission-line profile of [O III] for a typical double-shell planetary nebula model of intermediate age. The maximum of the surface brightness marks the inner edge of the nebula, i.e. the spatial position of the contact surface which is separating the shocked central-star wind from the nebular matter. The line-profile peaks are associated with those (radial) positions where the emission becomes the largest, after proper weighting with the electron density and the density of the ion in question. Usually the two strong line peaks belong to the rim because of its high density as compared to the shell whose signature are the weak “bumps” on either side of the strong components.

Note that, while the positions of the two shock fronts can be determined from the surface brightness distribution, the corresponding flow velocities immediately behind these fronts cannot in general be deduced from line profiles because of the combined influence of the radial density and velocity gradients. This fact is of importance for certain applications, e.g. for the discussion of expansion parallaxes (cf. Mellema 2004).

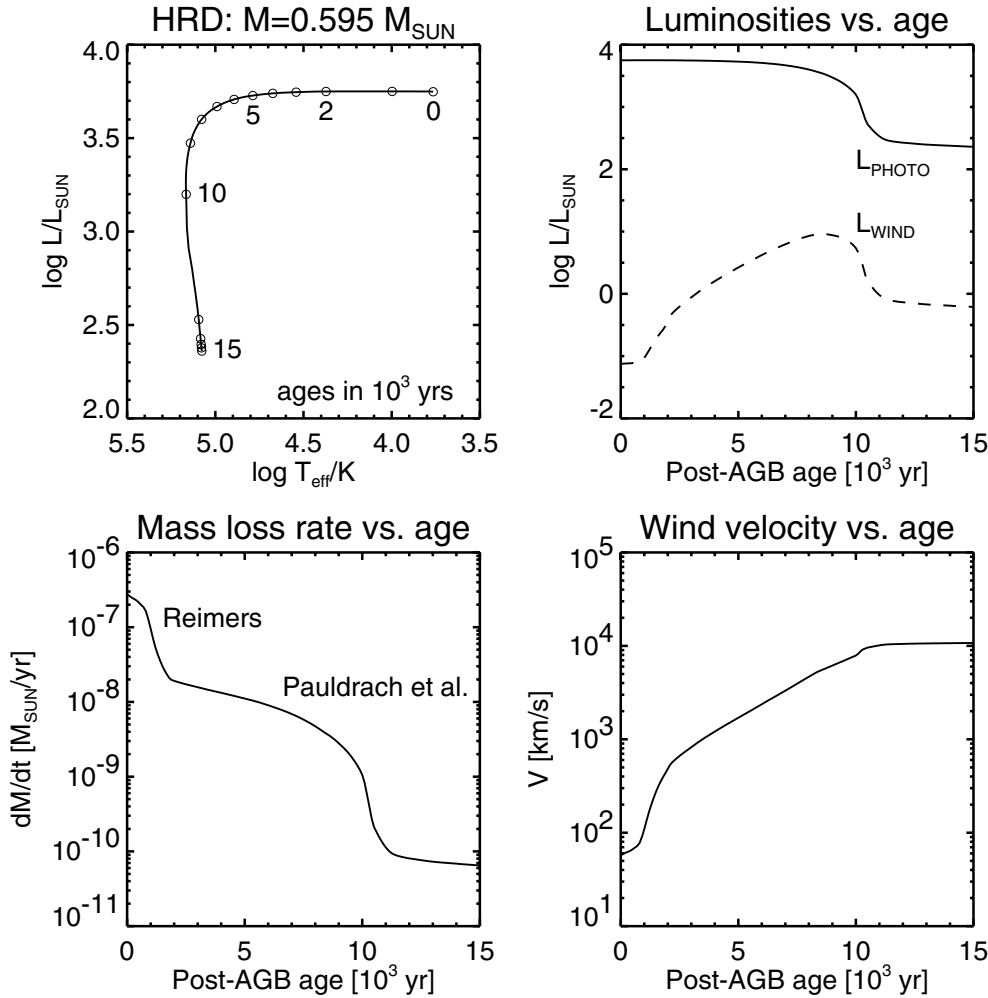


**Fig. 1.** *Top:* evolutionary path for the  $0.595 M_{\odot}$  post-AGB model with ages indicated (*left*), and the corresponding photon and wind luminosity,  $M \cdot V^2/2$  (dashed line) vs. time (*right*). *Bottom:* mass-loss rate (*left*) and wind velocity (*right*). We followed the recommendations of Pauldrach et al. (1988) for the parameters of the central-star wind, while we assumed a Reimers’ wind (Reimers 1975) during the short transition region from the AGB to the planetary-nebula domain (see also Paper I).

## 2.1. General discussion of the models

An illustration of the properties of our models and how they depend on the chosen  $\alpha$  is given in the Figs. A.1 and A.2 displayed in the Appendix A. For the purpose of the present discussion of the models, only their champagne phase of expansion is of relevance. The sequence of models with different initial density gradients of the ambient AGB wind as shown in these figures illustrates nicely how structure and expansion speed depend on  $\alpha$ .

Firstly it can be noted that the speed of the outer shock increases with  $\alpha$ , and that the velocity jump across the shock front increases as well, from about 5 to about  $37 \text{ km s}^{-1}$  for  $\alpha = 3.5^1$ . Likewise, the shell becomes more and more diluted, with density gradients changing slowly from positive to negative values above  $\alpha \approx 2.5$ . The inner parts of the models remain wind compressed and constitute a dense rim for all  $\alpha$  and all times, and the rim matter is accelerated to values comparable to the postshock speeds when the central star reaches the turn-around point.

<sup>1</sup> Figure A.1 may give the impression that during the earlier phases of evolution the models with larger  $\alpha$  are falling *behind* those with smaller  $\alpha$ . But the smaller sizes of the former for a given age are only caused by a longer duration of the optical thick stage with relatively low expansion speeds.

An important consequence of the structural changes caused by different  $\alpha$  is seen in the radial surface brightness distribution of the shell (right panels of Figs. A.1 and A.2): the concave shape becomes more linear for  $\alpha \gtrsim 3$ , together with a systematic increase of the rim-to-shell density resp. brightness contrast. The brightness contrast between the AGB wind (the “halo”) and the shell increases considerably with  $\alpha$ , too. Our models indicate that double shell planetary nebulae which show a linearly decreasing shell brightness must expand into an AGB wind with an initial density power law index of at least  $\alpha \approx 3$ . This is only possible if *the AGB mass-loss rate has increased substantially towards the end of the AGB evolution*.

During the early phases of evolution the rim cannot keep pace with the shell, and thus the shell-to-rim size ratio increases with  $\alpha$ . As said earlier, the rim constitutes a wind blown bubble whose expansion depends on the power of the wind and the density of the ambient matter (the shell’s density ahead of the rim’s shock), which both are variable in time. Our simulations shown in Figs. A.1 and A.2 indicate the following: for the models with  $\alpha \lesssim 2.5$  the shell-to-rim size ratios decrease during the course of evolution to values well below 1.4, a value too small if compared with the observational data (cf. Fig. 24 in Paper I). Only for models that expand in an environment with an initial  $\alpha \gtrsim 3$  the shell-to-rim size ratio remains always above 1.5.

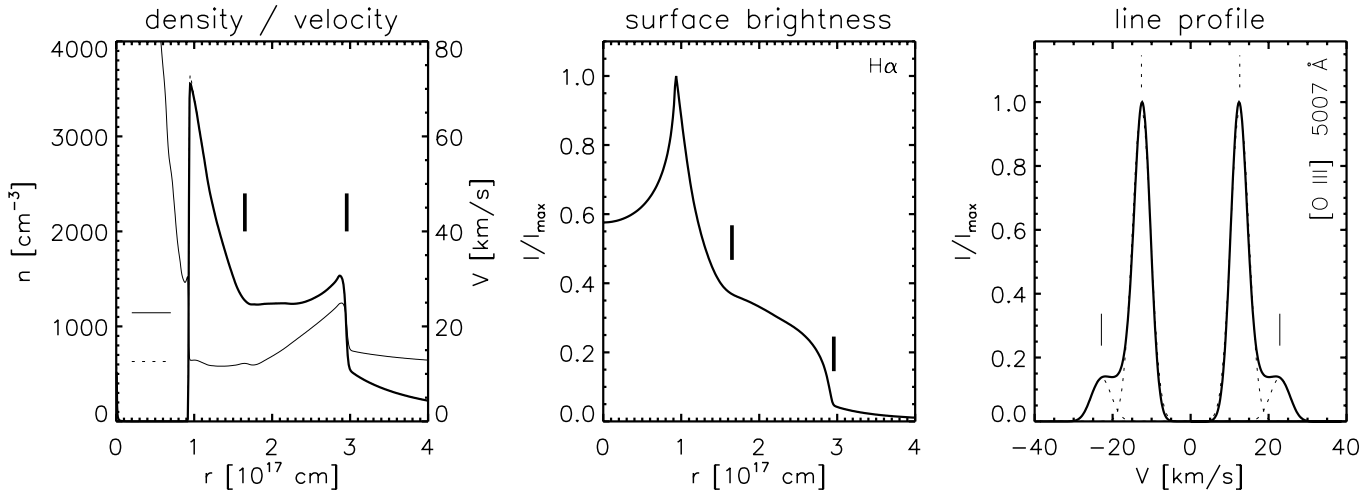


**Fig. 2.** Radial dependence of heavy-particle number density (thick) and velocity (thin) (*left*),  $H\alpha$  surface brightness (*middle*), and central emission-line profile of  $[O\ III] 5007 \text{ \AA}$  (*right*), both normalized to their maximum emission, of a hydrodynamical model with age of 4204 yr,  $\alpha = 2.5$ , and central-star parameters of  $M = 0.595 M_{\odot}$ ,  $L = 5463 L_{\odot}$  and  $T_{\text{eff}} = 49941 \text{ K}$ . In the structure and surface-brightness plots, the positions of the leading shock fronts of the rim and the shell are indicated by thick vertical marks, while the thin horizontal marks in the structure panel correspond to the vertical marks in the profile panel indicating the velocities within the respective shells as they result from our decomposition of the emission-line profile (right, dotted profiles). The latter are computed with a circular numerical aperture of  $1 \times 10^{16}$  cm radius.

Figure A.3 illustrates the appearance of the emission-line profiles of  $[N\ II]$  and  $[O\ III]$  as seen through the center of the resp. model nebulae. The main line components are the signature of the dense inner nebular parts, i.e. of the rims. During the rather early phase of evolution selected for this figure, the flow velocities within the rims are still quite slow, as indicated by the small line splits, especially for the models with large  $\alpha$ . The signature of the faster flowing shell material are weak shoulders which become nearly undetectable for the faster expanding models because of their higher degree of dilution.

Note that for large  $\alpha$  the high intensity contrast between the rim and shell and the slow expansion rate of the rim is also a consequence of the initial density structure chosen: with power-law density distributions models with large  $\alpha$  have more mass closer to the star as compared to models with smaller  $\alpha$ .

## 2.2. The $\alpha = 2$ cases

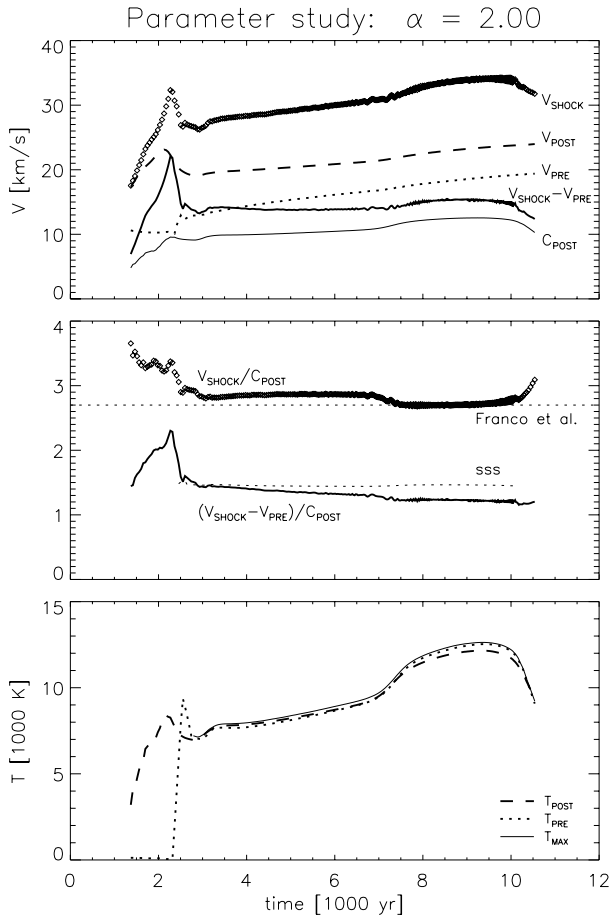
Here we discuss the flow properties of model sequences for the standard case of a stationary outflow until the mass-loss is shut down ( $\alpha = 2$  cases), and we utilize the model with the  $0.595 M_{\odot}$  central-star as a reference sequence. The AGB mass-loss rate is  $4.3 \times 10^{-5} M_{\odot} \text{ yr}^{-1}$ , with the initially constant wind velocity of  $V_{\text{agb}} = 10 \text{ km s}^{-1}$ .

Figure 3 illustrates how the expansion properties of this model nebula develop with time which is typical for the general evolution of planetary nebulae: at the beginning we have the optically thick phase where the ionization front is trapped and drives a shock wave into the ambient neutral AGB wind (D-type ionization front). The increasing electron temperature in the ionized region accelerates the shock steadily up to  $33 \text{ km s}^{-1}$  until the ionization front overtakes the shock. The front is now decelerated to  $27 \text{ km s}^{-1}$  because of the pressure

increase in the AGB flow ahead of it, and the flow enters the champagne phase for completely ionized gases under nearly isothermal conditions (cf. Fig. 3, bottom panel). The speed of the shock increases slowly with time and proportional to the sound speed until recombination occurs at about 10 000 yrs after the beginning of the simulation. Electron temperature and sound speed are then reduced, and hence the shock is slowed down correspondingly. The “jumps” in the shock front speed seen at  $t = 3000$  and  $t = 7500$  yrs are due to corresponding jumps of the electron temperature caused by additional heating after the passage of the He I and the He II ionization fronts.

During the transition optically thick/thin the AGB wind speed,  $V_{\text{pre}}$ , increases rapidly from 10 to  $13 \text{ km s}^{-1}$ , and after complete ionization the AGB wind is steadily accelerated by its own pressure gradient, which gives  $\dot{V}_{\text{pre}} = \alpha \cdot C_{\text{pre}}^2 / r$  for power-law density distributions. The relative motion of the front decreases only slowly and remains later virtually constant, and the velocity jump across the shock as well (compare  $V_{\text{post}}$  with  $V_{\text{pre}}$  in the top panel of Fig. 3).

This behaviour can be explained within the frame of self-similar isothermal flows discussed in the introduction. We solved the differential equations for self-similar solutions like in Chevalier (1997), with the difference that we imposed at every time the actual  $V_{\text{pre}}$  from our numerical solution as outer boundary condition. The resulting self-similar solutions (sss) are plotted as a dashed line in Fig. 3 (middle). At early times of the champagne flow,  $t \lesssim 4000$  yr, our numerical result agrees very well with the self-similar solution, viz.  $(V_{\text{shock}} - V_{\text{pre}}) / C_{\text{post}} = 1.45$ . Later the shock front falls a little bit behind because the ideal conditions necessary for self-similar solutions are not completely met by our model. For instance, the electron temperature and hence the sound speed increases with time because of the temperature evolution of the central star



**Fig. 3.** Expansion properties of a nebular model with the initial parameters  $\alpha = 2$  and  $V_{\text{agb}} = 10 \text{ km s}^{-1}$  coupled to the  $0.595 M_{\odot}$  post-AGB stellar model and plotted vs. age of the model. *Top:* velocities, in the stellar frame, of the outer (i.e. the shell's) shock front,  $V_{\text{shock}}$ , of the AGB wind immediately before the front,  $V_{\text{pre}}$ , of the gas behind the front,  $V_{\text{post}}$ , and of the difference velocity,  $V_{\text{shock}} - V_{\text{pre}}$ . The (isothermal) sound speed,  $C_{\text{post}}$ , is given for comparison. The subscript “post” refers to the maximum velocity reached after the passage of the shock front, corresponding to the end of the shock’s relaxation zone. *Middle:* absolute and relative shock-front speeds in units of  $C_{\text{post}}$ , compared with the approximate solution of Franco et al. (1990) and the self-similar solution for isothermal expansion (sss). *Bottom:* electron temperatures in front of and behind the outer shock,  $T_{\text{pre}}$  and  $T_{\text{post}}$ , and the maximum temperature,  $T_{\text{max}}$ , reached within the shock relaxation zone.

(Fig. 3, bottom). We will come back to this point in Sect. 3 where we will see that the expanding shock of our model with  $\alpha = 2$  obeys closely but not completely the isothermal jump condition.

For completeness we show in Fig. 3 (middle) also the approximate solution of Franco et al. (1990). Although their solution assumes the medium to be initially in rest, the agreement with our simulations is also quite good. An initially constant flow velocity has obviously only a minor influence on the final flow properties.

The bottom panel of Fig. 3 illustrates the behaviour of the electron temperatures ahead of and behind the shock, together with the maximum temperature reached due to the gas

compression by the shock. One notices that the electron temperatures before and behind the shock do not match exactly. This is a consequence of our fully time-dependent calculations: recombination and cooling time scales depend on the electron densities and differ therefore in the ionized AGB wind (the halo) and in the shock compressed, denser nebular matter. This discrepancy becomes larger at later evolutionary phases because of the then generally lower densities. In PNe, the electron temperatures are fully controlled by radiative processes, and the passage of a shock is only a minor disturbance, at least in the  $\alpha = 2$  case where the shock is weak.

The shock jump conditions contain only pressure and density ratios and should thus be independent of the mass-loss rate, hence density, of circumstellar envelopes. The self-similar solutions for power-law density distributions predict that the shock speed is only weakly dependent on the initial flow speed (Chevalier 1997) but strongly dependent on the density gradient and becomes infinite for  $\alpha \rightarrow 3$  (Shu et al. 2002). We used 9 model sequences from Paper I which have a variety of envelope configurations and central stars, and plotted their flow properties in Fig. 4. The density of the envelopes is characterized by  $\dot{M}_{\text{agb}}/V_{\text{agb}}$  of the initial envelope configurations. The top panel of this figure shows the mean accelerations of the shocks driven by D-type ionization fronts for the different models. The dependence on the envelope structure and central star evolution is as expected: the shock acceleration increases with decreasing mass density of the AGB wind for a given central star, but depends also on the temperature evolution time scale of the star. Less massive and thus more slowly evolving stars heat the gas and thereby accelerate the shock also more slowly. Despite the different accelerations, all the models end up finally with about the same maximum shock speed relative to the preshock flow,  $V_{\text{shock}} - V_{\text{pre}} \approx 2.2 C_{\text{post}}$ .

All model sequences (except one) enter later their champagne phase with a very unified expansion behaviour,  $V_{\text{shock}} - V_{\text{pre}} \approx 1.4 C_{\text{post}}$ , measured shortly after the ionization front has overtaken the shock (Fig. 4 bottom panel), and in good agreement with the result for self-similar isothermal flows discussed earlier. Like the relative shock velocity itself, also the relative postshock velocity is practically the same for all sequences,  $V_{\text{post}} - V_{\text{pre}} \approx 0.6 C_{\text{post}}$ .

From our numerical simulations we conclude that, for  $\alpha = 2$ , the expansion of a planetary nebula into a stationary AGB outflow is reasonably well described by self-similar hydrodynamical flows under isothermal conditions. As a consequence, the nebular expansion rate (in the stellar frame) as given by the speed of its outer shock front is expected to be rather small: according to Fig. 3 it reaches marginally  $35 \text{ km s}^{-1}$  at the end of the evolution, and the postshock flow speed,  $V_{\text{post}}$ , which is about  $10 \text{ km s}^{-1}$  lower, only  $24 \text{ km s}^{-1}$ . Note that this conclusion rests on the assumption of an initial AGB wind speed of  $10 \text{ km s}^{-1}$ . Increasing this value to, say  $15 \text{ km s}^{-1}$  would increase the nebular expansion rate by  $\lesssim 5 \text{ km s}^{-1}$ .

Considering that (i) the spectroscopically measurable flow expansion is even somewhat below  $V_{\text{post}}$  because of the (always positive) velocity gradient within the expanding shell, that (ii) the electron temperature of our models is in good agreement with observations, that (iii) AGB wind speeds are

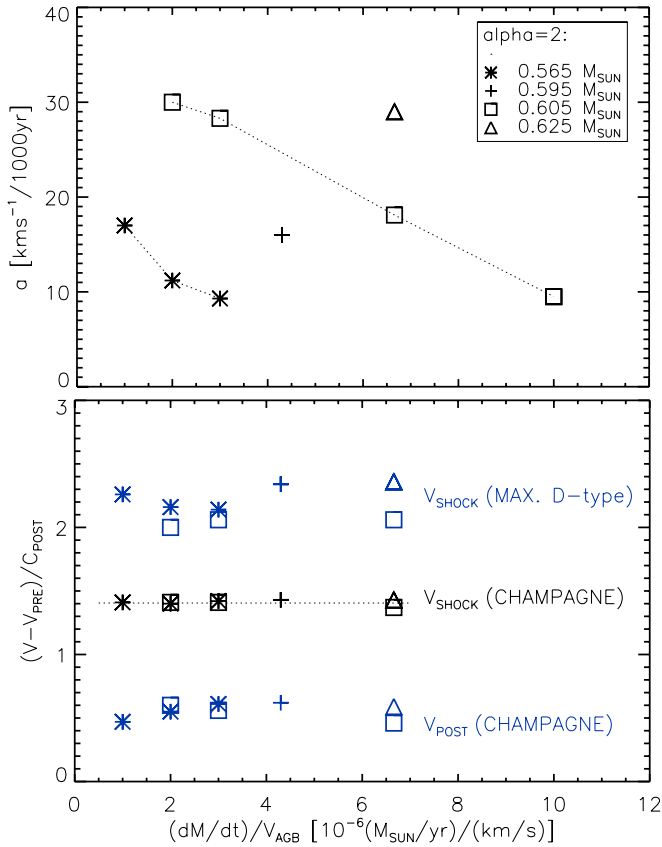


**Fig. 4.** *Top:* mean accelerations of shocks driven by D-type ionization fronts vs.  $\dot{M}_{\text{agb}}/V_{\text{agb}}$  of the initial model envelopes with  $\alpha = 2$  and for various central-star masses as given in the legend. The hydrodynamical sequences are those from Paper I (Table 1 therein) supplemented by the new reference sequence for  $M = 0.595 M_{\odot}$  (plus sign). The number of data points belonging to a particular central-star model reflects the different number of models computed for each central-star model. *Bottom:* for the same model sequences, the maximum shock velocities at the end of the acceleration phase, those immediately after the beginning of the champagne expansion phase, and the post-shock flow velocities, all of them relative to the AGB flow and in units of  $C_{\text{post}}$ , are plotted against  $\dot{M}_{\text{agb}}/V_{\text{agb}}$ . The values plotted are taken during the early phase of the champagne expansion, and the horizontal dotted line is the mean value, 1.4. The model with the highest initial density ( $\dot{M}_{\text{agb}} = 1 \times 10^{-4} M_{\odot} \text{ yr}^{-1}$  and  $V_{\text{agb}} = 10 \text{ km s}^{-1}$ ) does not become optically thin and thus cannot be plotted here.

limited to values below  $20 \text{ km s}^{-1}$ , and that (iv) the measured flow speed of the shell reaches up to  $40 \text{ km s}^{-1}$  (see Sect. 4), we conclude further that generally all nebular models with  $\alpha = 2$  are *not* suited to describe real objects. The only alternative is to assume larger density gradients for the circumstellar matter, and this possibility will be addressed in some detail in the following section.

### 3. Circumstellar environment and expansion speed

#### 3.1. Flow properties

We restrict our investigation of the models with various power-law density distributions to sequences computed for only one

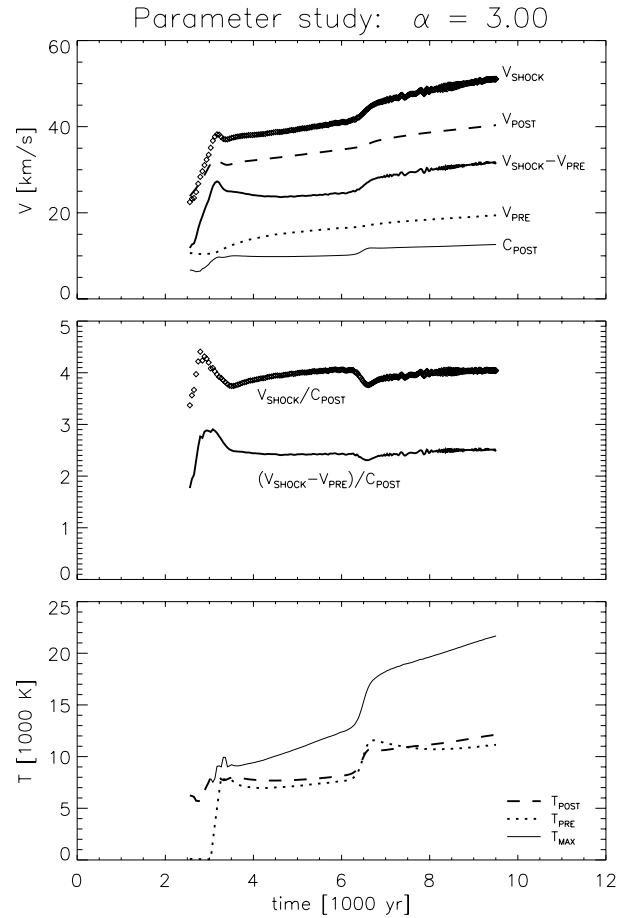


**Fig. 5.** Same as in Fig. 3, but for  $\alpha = 3$ .

particular central star, viz.  $0.595 M_{\odot}$ , since all the relevant flow properties during the champagne phase of evolution are expected also to be independent of the central star as long as the flow has time to adjust to the actual stellar parameters. Given the rather long evolutionary time scale of this central-star model, this approach is fully justified.

As an example we show in Fig. 5 the expansion behaviour of a model with  $\alpha = 3$ . The outer shock propagates much faster than in the  $\alpha = 2$  case, is considerably stronger, and the velocity jump is about  $20 \text{ km s}^{-1}$  or  $\approx 2 C_{\text{post}}$  instead of  $\approx 0.6 C_{\text{post}}$ . After 10 000 years,  $V_{\text{post}}$  reaches about  $40 \text{ km s}^{-1}$ , to be compared with only  $24 \text{ km s}^{-1}$  in the  $\alpha = 2$  case. The relative shock speed,  $V_{\text{shock}} - V_{\text{pre}}$ , is now increasing slightly with time during the champagne phase, from  $23 \text{ km s}^{-1}$  (or  $\approx 2.3$  in terms of the isothermal sound speed,  $C_{\text{post}}$ ), to  $32 \text{ km s}^{-1}$  (or  $2.6 C_{\text{post}}$ ).

Our numerical model with  $\alpha = 3$  does not comply with the self-similar solution since the latter predicts an infinite shock speed. The reason is that due to the larger shock strength the compressional heating becomes now significant, as is seen in the high value of  $T_{\text{max}}$  which exceeds  $20\,000 \text{ K}$  during the course of evolution (Fig. 5, bottom panel). The shock cannot be considered as isothermal, and its speed is reduced to a finite value accordingly. The radiative cooling, however, is so efficient that the shock's relaxation zone is small and the main nebular body nearly isothermal. The width of this relaxation

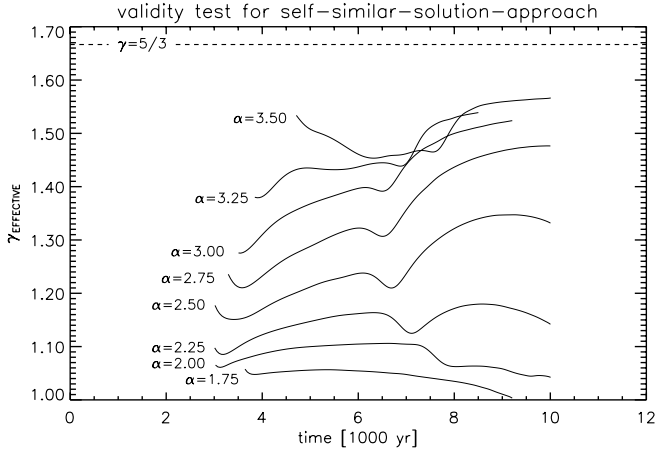


**Fig. 6.** Temporal variations of the *effective adiabatic exponent*,  $\gamma_{\text{eff}}$ , for our model sequences with different  $\alpha$ , computed during the champagne expansion phase from Eq. (2) with the actual density and pressure ratios across the outer shock. The adiabatic case ( $\gamma = 5/3$ ) is indicated by the dashed horizontal line. The dip visible in nearly all cases is caused by the passage of the He II ionization front.

regime is  $7 \times 10^{16}$  cm, or only 6% of the shell radius at age 10 000 years.

By introducing an *effective adiabatic exponent*,  $\gamma_{\text{eff}}$ , we can conveniently investigate whether the outer shock behaves isothermal or not. Using the jump condition for adiabatic shocks,

$$\rho_2/\rho_1 = \frac{(\gamma - 1)P_1 + (\gamma + 1)P_2}{(\gamma + 1)P_1 + (\gamma - 1)P_2}, \quad (1)$$

we solve for  $\gamma = \gamma_{\text{eff}}$ ,

$$\gamma_{\text{eff}} = \frac{(\rho_2/\rho_1 + 1)(P_2/P_1 - 1)}{(\rho_2/\rho_1 - 1)(P_2/P_1 + 1)}, \quad (2)$$

and insert the actual ratios of pressure and densities across the front. The index “1” refers to values immediately in front of the shock, while the relevant postshock values,  $\rho_2$  and  $P_2$ , are taken at the position of  $T_{\text{max}}$ . Figure 6 shows the result.

There appears a clear tendency of increasing deviations from the isothermal shock conditions with increasing  $\alpha$ . For  $\alpha \lesssim 2$  the isothermal assumption ( $\gamma = 1$ ) is rather good, and the self-similar flow solutions are a useful tool to describe the expansion of planetaries. This approximation becomes increasingly poor for  $\alpha > 2$ , and breaks down completely if  $\alpha \gtrsim 3$ . The general expansion behaviour of the shell’s front for different  $\alpha$  is illustrated in Fig. 7 which gives the mean acceleration of the shock during the optically thick phase (D-type ionization front, top panel), the maximum velocity achieved thereby, and the velocities of the shock and the postshock flow at the beginning of the champagne phase of evolution (bottom panel). All velocities plotted are relative to the ambient AGB wind and normalized to the postshock sound speed. All postshock values (including the sound speed) are taken at a radial position immediately *behind* the relaxation zone of the shock. The expansion velocities vary during the course of evolution (cf. Figs. 3 and 5), but their total variation is rather small and thus neglected.

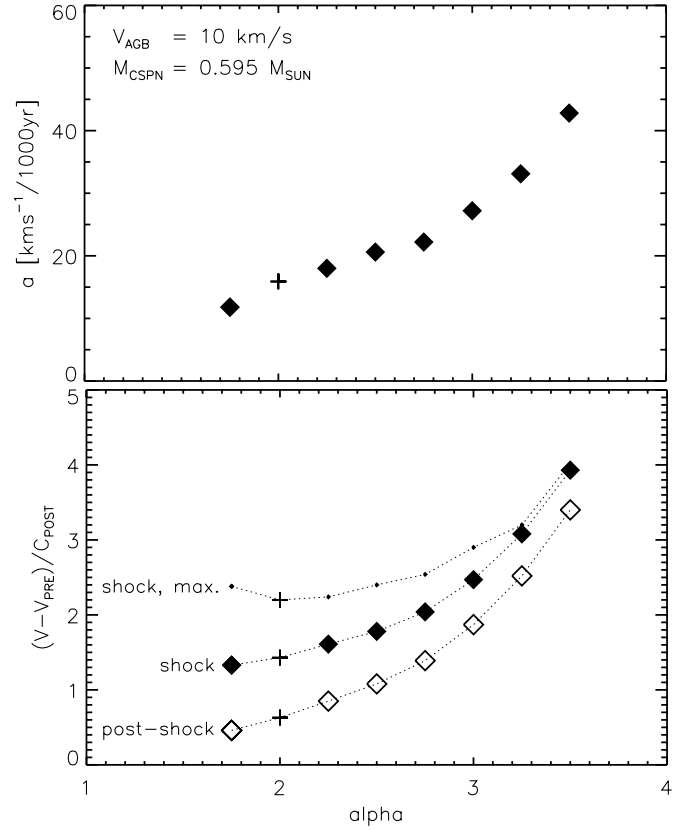


**Fig. 7.** *Top:* mean accelerations of the shock driven by a D-type ionization front for different  $\alpha$ . All the models have initially  $n = 10^5 \text{ cm}^{-3}$  at  $r = 3 \times 10^{16}$  cm,  $V_{\text{agb}} = 10 \text{ km s}^{-1}$  and are coupled to the  $0.595 M_{\odot}$  central-star. *Bottom:* the same models at the beginning of their champagne phase of evolution. Given are the shock front speeds and their corresponding postshock flow velocities, both relative to the AGB flow, and in terms of the postshock sound speed. For comparison, the maximum speed (in units of the postshock sound speed) achieved during the acceleration phase is also plotted. – In both panels our standard sequence ( $\alpha = 2$ ) is marked by the plus sign.

While the expansion for  $\alpha \lesssim 2$  follows rather closely the predictions of self-similar flow solutions for isothermal conditions, the situation is different for larger  $\alpha$ . The shock speed is reduced due to the increasing departure from the isothermal shock conditions (Fig. 6) and remains finite. Still, the expansion speed increases considerably if  $\alpha$  approaches and surpasses 3, and because of the increasing shock strength the speed of the shock-compressed matter comes closer to that of the front. It is obvious from these models that the expansion velocities as they are observed in planetary nebulae can only be reached if the density distribution of the ambient AGB matter had initially a slope corresponding to a power-law distribution with  $\alpha \gtrsim 3$ . Similarity solutions of the flow equations for isothermal gases are in general not applicable to real PNe.

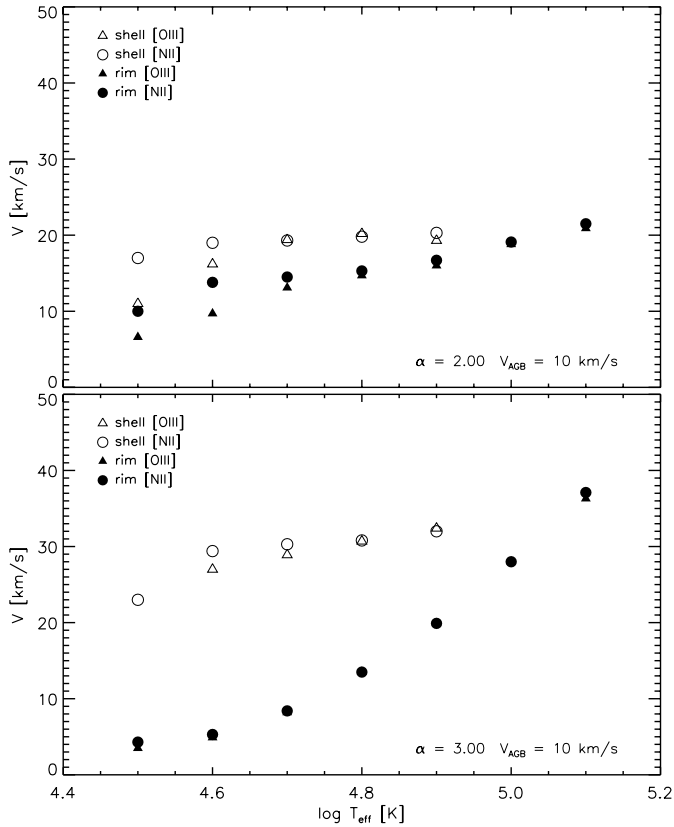


**Fig. 8.** Doppler expansion velocities for the shell and the rim as they follow from a decomposition of the computed line profiles of [N II] 6583 Å (circles) and [O III] 5007 Å (triangles) vs. the effective temperature of the central star for  $\alpha = 2$  (top) and  $\alpha = 3$  (bottom). Open symbols are for the shell, filled symbols for the rim. The velocities derived from these two ions can be different because of different ionic stratifications. If shell and rim velocities are about the same, the former is not measurable because of blending, considering the fact that the rim density is so much higher than the shell density.

### 3.2. Doppler velocities

From the individual models we computed emission-line profiles and determined the flow properties of the shell and the rim from the Doppler splits as outlined earlier in Sect. 2. Note that by means of the Doppler splits one measures the velocity of the bulk matter within the resp. shells, appropriate weighting over the density and ionization fraction distribution along the line of sight included. Thus the resulting velocities do depend on the nebular structure and are in general *not* indicative of the velocity immediately behind a shock front. The “measured” expansions of the models are shown in Fig. 8 for two sequences,  $\alpha = 2.0$  and  $\alpha = 3.0$ . Because we want to compare our models with the expansion properties of real objects, we used the effective temperature of the central star as a distance-independent proxy for the evolutionary state (or age) of the model.

We determined the observable expansion properties of our model planetaries from the strong [N II] and [O III] lines in order to illustrate the differences especially during the early phase of evolution when the ionization of nitrogen and oxygen is very

different. The nitrogen line has the tendency to indicate larger velocities in the shell because singly ionized nitrogen is more prominent in the outer, faster moving parts of the shell. During the later phases where both the rim and the shell velocities are very close to each other, the latter one is not plotted since the rather weak shell emission cannot be disentangled from the total profile dominated by the rim emission. As one expects from Figs. 3 and 5, the “measured” velocities of the  $\alpha = 2$  sequences are falling well behind those of the  $\alpha = 3$  sequence. As a consequence of the radial density and velocity profile, these “measured” shell velocities are generally lower than the postshock velocities shown in Figs. 3 and 5. They barely exceed  $30 \text{ km s}^{-1}$  in the  $\alpha = 3$ , whereas the postshock velocity reaches more than  $40 \text{ km s}^{-1}$ , as shown in Sect. 3.1, Fig. 5.

The rim, as a wind-blown bubble, accelerates considerably for larger density gradients because it expands into a more diluted shell. Although it starts with a very low velocity because the matter at the inner edge of the ionized region is effectively braked by the pressure of the ionized gas, it may become even faster than the shell during the final phase of evolution (cf. bottom panel of Fig. 8). We emphasize again that the expansion property of the rim does not only depend on the density of the ambient matter, but also on the central-star wind and its variation with the stellar parameters. The increase of the wind power with time is responsible for the rim acceleration, and the common assumption of a constant rim speed is not tenable for PN evolution. We recall here that the wind properties are the same in all models used in this work ( $M = 0.595 M_{\odot}$ , see Fig. 1).

## 4. Observational constraints

The model calculations discussed in the previous sections clearly demonstrate how the expansion properties depend on the radial density distribution set up earlier by the AGB wind. Spectroscopic measurements of the shell’s expansion speed would thus constrain the density profile of the AGB wind and thus the time dependence of the mass-loss rate for a brief time span during the very end of the AGB evolution that is unobservable otherwise. Unfortunately, the shell emission is very often weak and difficult to observe and has thus escaped detection until the introduction of sensitive semiconductor detectors (Chu et al. 1984). Available catalogues (cf. Weinberger 1989) list only velocities deduced from the bright line components which belong to the rim and are by no means indicative for the general expansion of the PN in question.

Some recent efforts were devoted to disentangle the full velocity fields in planetary nebulae by high-resolution spectroscopy (e.g. Gesicki et al. 1996; Neiner et al. 2000; Gesicki et al. 2003), but these studies do not provide individual bulk velocities useful for a comparison with our hydrodynamics models. Thus we decided to get additional high-resolution spectra of selected objects with well developed shells and rims which do not deviate too much from a spherical shape. We determined from the line profiles the velocities of the rim and the shell by Gaussian fitting in the same way as we did it for the theoretical profiles from the model sequences, utilizing only the

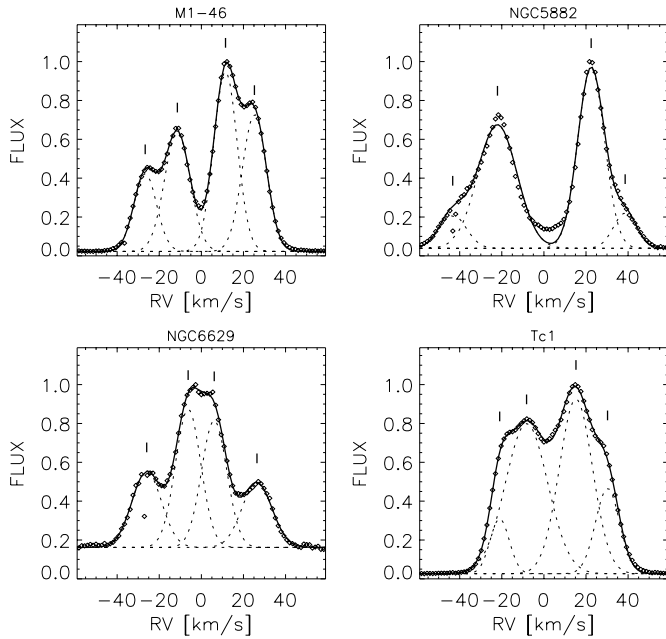


**Fig. 9.** Normalized high-resolution line profiles of [N II] 6583 Å taken with the CAT at the 3.5 m telescope in La Silla, Chile (dots). The fit is given by the line, together with the individual Gaussian components (dashed).

strong [O III] and/or [N II] lines with the highest signal-to-noise ratio.

We selected for the present study only nebulae with hydrogen-rich central stars since the evolution of central stars of the Wolf-Rayet spectral class is still not understood and certainly not represented by the models used in this work.

#### 4.1. The observations and their reduction

##### 4.1.1. The CAT data

The observations were performed in June 1998 at the ESO CAT telescope, a subsidiary 1.4 m telescope feeding into the Coude Echelle Spectrometer (CES) located at the neighbouring 3.6 m telescope. We used the “long camera” (f/4.7) giving a resolving power of 60 000 ( $5 \text{ km s}^{-1}$ ). The slit aperture was  $2''$ . The spectra cover one order of the echelle, including  $H\alpha$  6563 Å and the [N II] 6583 and 6548 Å lines. The effective integration times cover 3 to 5 hours. The spectra were reduced in the usual way by using the MIDAS package (bias subtraction, flat field correction, wavelength calibration).

The reduced line profiles for the strong [N II] lines are shown in Fig. 9, together with their Gaussian components, and the individual velocities are listed in Table 2.

##### 4.1.2. NTT and NOT data

High-resolution long-slit spectra of selected PNe were obtained at two telescopes: the 3.5 m NTT/ESO telescope at La Silla, Chile, on the nights of January 21 and 22, 1999, and the 2.6 m Nordic Optical Telescope (NOT) at La Palma, Spain, on December 21 and 22, 1999.

**Table 2.** Individual Doppler velocities from the CAT data.

Object	$V_{\text{rim}} / \text{km s}^{-1}$		$V_{\text{shell}} / \text{km s}^{-1}$	
	6548 Å	6583 Å	6548 Å	6583 Å
M 1-46	11.6	11.4	26.0	25.9
NGC 5882	22.7	22.3	37.9	41.2
NGC 6629	–	6.2	27.6	26.2
Tc 1	11.5	11.7	25.6	25.6

At the NTT, we used the EMMI spectrograph in its long-slit, high-resolution mode (grating #14), providing a spectral resolving power of  $\lambda/\Delta\lambda = 70\,000$  with the adopted slit width  $0''.8$ . The slit length was of  $6'$ . With the TEK 2048<sup>2</sup> CCD ESO #36 detector, the spatial scale of the instrument was  $0''.27 \text{ pix}^{-1}$ . The seeing during the observations was between  $1''.1$  and  $1''.8$  full width at half-maximum (*FWHM*). Narrow-band filters were used to isolate two echelle spectral orders; first, a 60 min spectrum (split into two sub-exposures) was taken in a region containing  $H\alpha$  6563 Å, the [N II] doublet at 6548 and 6583 Å, and the fainter He II line at 6560 Å, and then another 60 min spectrum was obtained in a spectral region centered on the [O III] 5007 Å line.

We observed the following nebulae (in parenthesis the adopted position angle of the slit): NGC 1535 (PA =  $+20^\circ$ ), IC 2448 ( $-44^\circ, +46^\circ$ ), NGC 2610 ( $0^\circ$ , only [O III] observations, 80 min in total), and My 60 ( $-50^\circ$ ).

At the NOT, we used the echelle spectrograph IACUB. The detector was a Thompson THX31156 1024 CCD, giving a spatial scale of  $0''.14 \text{ pix}^{-1}$ . The projected slit width was  $0''.4$ , providing a spectral resolution of 50 000. The seeing during observations was around  $1''$ . Like at the NTT, two narrow-band filters were used to select spectral regions around the  $H\alpha$  and the [O III] lines. Exposure times ranged from 15 min to 120 min depending on the surface brightness of the nebulae.

The PNe observed at the NOT were IC 418 (PA =  $+60^\circ, -30^\circ$ ), NGC 3242 ( $+60^\circ, -20^\circ$ ), and NGC 7662 ( $+48^\circ, +138^\circ$ , only [O III] observations).

Example profiles of all the observed objects are shown in Fig. 10, and the deduced velocities are given in Table 3. In three cases (NGC 1535, NGC 2610, and NGC 7662) we can *not* see in Fig. 10 faint signatures of the shell emission in the outer wings of the line profiles, which is an indication that the rim moves with similar or even higher speed than the shell. The latter case seems indeed evident for NGC 1535 from inspection of the long-slit spectrograms taken by Sabbadin et al. (1984, Fig. 2 therein). However, our own long-slit spectra taken with the EMMI spectrograph have a much better spectral resolution and revealed a larger velocity of the shell matter: from the velocity ellipse we deduced  $V_{\text{shell}} = 27 \text{ km s}^{-1}$  which is only slightly larger than the value for the rim.

IC 418 is a typical young and still optically thick nebula, but we included it because this object should indicate the velocities typical during the early expansion phase. Such objects are expected to have large velocity differences within the ionized region (see Paper I), and the different line splitting seen

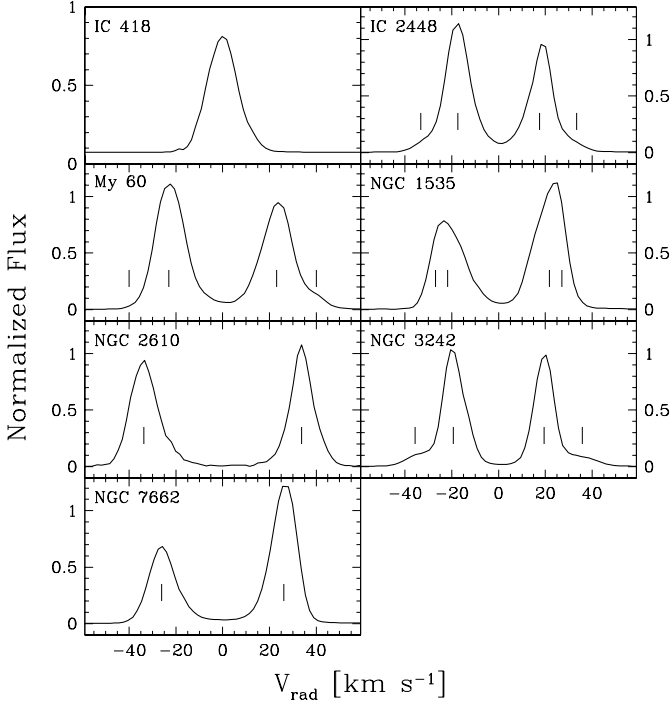


**Fig. 10.** Normalized high-resolution line profiles of [O III] 5007 Å for the PNe sample observed with NTT or NOT. The positions of the individual Gaussian components are indicated by the vertical bars (except for IC 418).

**Table 3.** Individual Doppler velocities from the NTT and NOT data.

Object	$V_{\text{rim}}/\text{km s}^{-1}$		$V_{\text{shell}}/\text{km s}^{-1}$	
	5007 Å	6583 Å	5007 Å	6583 Å
IC 418	5.0:	–	–	12.7
	–	–	–	12.4
IC 2448	17.1	17.5	33.5	–
	17.9	18.6	33.2	–
My 60	23.1	23.7	40:	–
NGC 1535	21.8	–	27.0	–
NGC 2610	33.7	–	–	–
NGC 3242	19.4	19.7	35.5	–
	19.5	–	36.0	–
NGC 7662	26.2	–	–	–
	26.0	–	–	–

in Fig. 11 are the result of this velocity gradient across the ionized shell. The [N II] lines probe the large flow velocity in the outer ionized regions close to the (D-type) ionization front, and are split accordingly, with  $V_{\text{shell}} = 12.5 \text{ km s}^{-1}$ . In contrast, the [O III] line, which originates very close to the inner regions of the shell, is not split at all. From the width of the [O III] line we estimate there a flow velocity not larger than about  $5 \text{ km s}^{-1}$  and interpret this value as typical for the early rim.

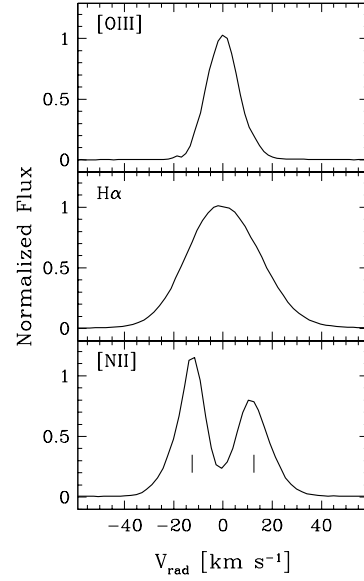


**Fig. 11.** Line profiles for the young PN IC 418.

**Table 4.** Combined data set of Doppler velocities of rim and shell deduced from the profiles of [O III] 4959/5007 Å and [N II] 6548/6583 Å.

Object	$V_{\text{rim}}/\text{km s}^{-1}$		$V_{\text{shell}}/\text{km s}^{-1}$		$T_{\text{eff}}/\text{K}$
	[O III]	[N II]	[O III]	[N II]	
IC 418	5.0:	–	–	12.5	36 000
IC 2448	17.5	18.0	33.3	–	65 000
M 1-46	–	11.5	–	26.0	45 000
My 60	23.1	23.7	40:	–	105 000
NGC 1535	21.8	–	27.0	–	70 000
NGC 2022	27.0	–	15:	–	100 000
NGC 2610	33.7	–	–	–	100 000
NGC 3242	19.5	19.7	35.7	–	75 000
NGC 5882	–	22.5	–	39.6	67 500
NGC 6629	–	6.2	–	26.9	47 000
NGC 6826	8.0	10.6	27.0	–	50 000
NGC 7662	26.1	–	–	–	100 000
Tc 1	–	11.7	–	25.6	47 500

The colon (:) indicates uncertain velocities that were estimated from Fig. 2 of Sabbadin et al. (1984), or from the unsplit [O III] line in the case of IC 418. The effective temperature of M 1-46 is from Guerrero et al. (1996).

## 4.2. Results

The combined two data sets from Tables 2 and 3 are shown in Table 4 together with the corresponding central star temperatures. We included NGC 6826 because its rim and shell velocities were available from the literature (Chu et al. 1984; Guerrero et al. 1998), and also NGC 2022 because one can estimate its shell velocity from the long-slit spectrograms taken by Sabbadin et al. (1984). The temperatures of the central stars are based on NLTE model atmosphere techniques if

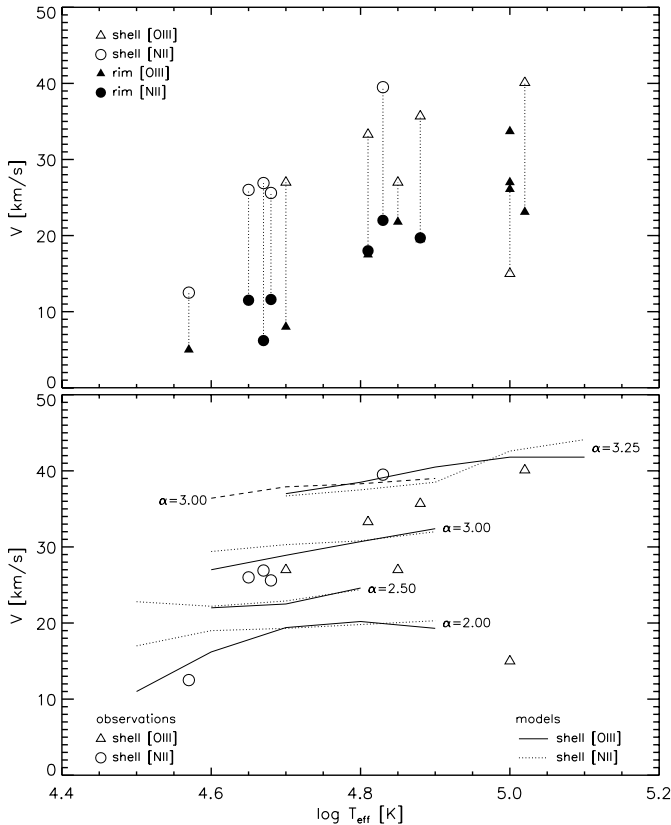


**Fig. 12.** *Top:* Doppler expansion velocities of the objects listed in Table 4 vs. the effective temperatures of their central stars. The symbols have the same meaning as in Fig. 8, i.e. open symbols are for the shell, filled ones for the rim. Velocities belonging to the same object are connected by dotted vertical lines. *Bottom:* comparison between the shell velocities (open symbols) displayed in the top panel and those found from our model sequences with various power-law density distributions as indicated. The dashed line belongs to the  $V_{\text{agb}} = 20 \text{ km s}^{-1}$  sequence ([O III] only); all other sequences have  $V_{\text{agb}} = 10 \text{ km s}^{-1}$ .

available (Méndez et al. 1992; McCarthy et al. 1997). In the four cases My 60, NGC 5882, NGC 7662, and Tc 1 we used the He II Zanstra temperatures (Gorny, priv. comm.).

The velocities of Table 4 are shown in the top panel of Fig. 12, plotted over  $T_{\text{eff}}$  of their central stars. We selected the stellar effective temperature as a distance-independent means to measure the age or evolutionary stage of an observed PN instead of some other distance-dependent quantity<sup>2</sup>. We assume thereby that all central stars with double-shell structures have very similar mass and evolution properties.

Figure 12 demonstrates clearly that both the rim and the shell experience a considerable acceleration with age (or with the effective temperature of the central star). The rim flow becomes nearly as fast as that of the shell during the course of

evolution, and is even faster in one case. The cases with no detectable shell Doppler split are among the most evolved objects with the hottest central stars. This is expected because similar flow speeds of rim and shell gas makes it difficult to disentangle the components of the line profile.

In the bottom panel of Fig. 12 the observed Doppler expansions of the individual shells are compared to the predictions of our power-law models. As expected from our previous findings (cf. Fig. 8), models with fixed AGB wind velocity and density power law index give only a very modest increase of the expansion speed with stellar effective temperature since the electron temperature of the shell (and hence the sound speed) depends only weakly on the stellar  $T_{\text{eff}}$  (Figs. 3 and 5). We note also that the expansion behavior of the models is virtually *independent* of the chosen central star mass as long as the evolution proceeds along the horizontal part of the HRD at nearly constant stellar luminosity.

As demonstrated by the dashed line for the  $\alpha = 3$  case, larger AGB wind velocities systematically increase the model's expansion speed. However, to explain the observed  $V_{\text{shell}} - T_{\text{eff}}$  relation, one would have to assume a variation of  $V_{\text{agb}}$  which is much larger than the observed range of AGB outflow velocities, and which is moreover correlated with the current effective temperature of the PN central star. A more likely explanation is that the effective density power law index  $\alpha$  increases systematically with  $T_{\text{eff}}$ , while the wind speeds at the tip of the AGB are not very different from object to object, clustering around  $V_{\text{agb}} = 10 \text{ km s}^{-1}$ .

In view of the fact that most objects of our observed sample have a similar morphological structure, we interpret the observed  $V_{\text{shell}} - T_{\text{eff}}$  relation as an evolutionary sequence and conclude that the expansion speed increases with *time* because of a steepening of the radial density gradient in the circumstellar wind envelope. During the early phases of the nebular evolution, i.e. when the outer shock is still close to the star,  $\alpha$  is about 2, but with increasing distance from the star  $\alpha$  changes gradually to a value of 3 or even larger, depending somewhat on the initial AGB wind velocity.

Within the frame of our models, the very low (but rather uncertain) shell velocity of NGC 2022 can be explained by a rather small density gradient ( $\alpha \lesssim 2$ ) throughout the whole AGB-wind envelope, possibly in conjunction with an initially slow AGB-wind velocity of  $V_{\text{agb}} \lesssim 10 \text{ km s}^{-1}$ . The rim's expansion is well in line with those of the rest of the sample.

The rim as a wind-blown bubble is driven into the ambient shell matter by the pressure of the hot shocked stellar-wind gas, and our models indicate only a modest dependence of the rim's expansion on the initial density stratification (see also Koo & McKee 1992). The observed Doppler expansion properties of the rims are rather well embraced by nebular models with density stratifications characterized with  $2 < \alpha \lesssim 3$  (cf. Fig. 8).

Note that all models have the same central star and correspondingly the same evolution of the wind parameters with time. The consistency of our models with the observed rim expansion properties indicates that the wind model employed by us is obviously rather close to reality.

<sup>2</sup> Partriarchi & Perinotto (1991) found a positive correlation between the expansion velocities of PNe and the wind velocities of their central stars. The use of the central-star wind speed is, however, not useful here because the wind parameters are not known for all objects listed in Table 4.

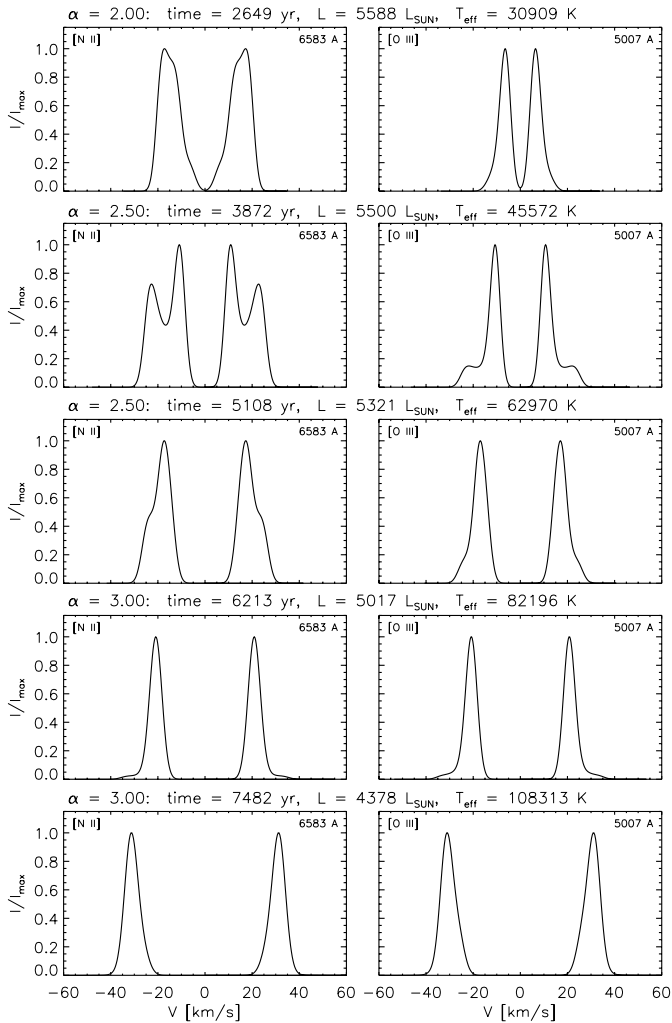


**Fig. 13.** Examples of emission-line profiles of [N II] and [O III] taken from our hydrodynamical sequences and selected such that they embrace the shapes of the observed profiles qualitatively. The model parameters are indicated above each panel. These profiles are again computed for the central line-of-sight using a numerical aperture of  $1 \times 10^{16}$  cm radius and with infinite spectral resolution.

As a consistency check we finally investigated whether the models with  $2 \lesssim \alpha \lesssim 3$  produce emission-line profiles consistent with the observed ones shown in Figs. 9 and 10. Therefore we plotted in Fig. 13 theoretical line profiles at selected positions along the sequences with  $\alpha = 2.0, 2.5$  and 3.

Considering that the theoretical profiles are not widened by instrumental effects, we see that they are able to match qualitatively the observed ones. The different speeds of the shell and the rim are clearly distinguishable, except for the most advanced example. These models cannot, of course, reproduce well the relative intensities and velocities of the components because our models started with somewhat arbitrary initial configurations with radius independent  $\alpha$ 's.

## 5. Discussion and conclusions

We have used an extensive grid of hydrodynamical model sequences with spherical geometry to study systematically the expansion properties of planetary nebulae with emphasis on their optically thin phase of evolution, which is also the main phase unless the central star is massive and evolving very fast. During this phase their morphology is determined by a double-shell structure consisting of a dense and bright rim surrounded by a more diluted and fainter shell. The rim is blown into the shell by the high pressure of the shocked central-star wind and obeys the rules of wind-blown bubbles. The shell is characterized by a champagne flow, i.e. it is thermally driven into the ambient stratified medium, and its expansion speed depends on the density *gradient* and the actual (isothermal) sound speed.

The dependence of the expansion properties of PNe as found by our model computations can be tested by means of real objects with known density stratifications. Unfortunately, only one determination of the density distribution of the AGB wind (the halo) does exist to date, viz. for NGC 6826 by Plait & Soker (1990). These authors found an  $\alpha' \approx 4$  power law for the (electron) density<sup>3</sup> and concluded, not much noticed then, that *the mass-loss rate increased very strongly with time*. Very recently Corradi et al. (2003a) came independently to the same conclusion while comparing the predictions of radiation-hydrodynamics calculations with the halo of NGC 6826.

The Doppler expansion of the shell is known by Chu et al. (1984) to be of  $27 \text{ km s}^{-1}$  (cf. Table 4), and by comparing this velocity with our models shown in Fig. 8 one arrives at  $\alpha \approx 3$ . This apparent discrepancy between  $\alpha'$  and  $\alpha$  can be explained by the fact that the AGB flow is accelerated by its own pressure gradient (cf. Sects. 2.2 and 3). From our models we find that an AGB flow with an initial density power law index of  $\alpha = 3$  steepens considerably after the AGB matter becomes completely ionized and can be described later by  $\alpha' \approx 3.7$ .

From our recently acquired halo image of NGC 6826 (Corradi et al. 2003b) we found a somewhat lower mean (logarithmic) brightness power law index of  $\beta \approx -5.5$ , which translate into  $\alpha' \approx 3.3$  (Schönberner et al. 2004). Given the uncertainties of the halo measurements and of the initial AGB-wind velocity, NGC 6826 thus shows satisfying agreement between its Doppler expansion measured from the shell gas and the radial density profile of the ambient halo matter.

The very low shell expansion rate of NGC 2022 discussed previously (Sect. 4.2) indicates that its halo must be different from that of NGC 6826. We thus measured the power law index of the halo surface brightness of our new H $\alpha$  image published recently by Corradi et al. (2003b) and found  $\beta \approx 3.3$ , which translates then into a radial run of the density with  $\alpha'$  slightly above 2. Thus we found also for NGC 2022 a reasonable consistency between the expansion speed of the shell and the density profile of the halo, roughly in line with our numerical simulations.

These two examples confirm that it is possible to determine the density stratifications of AGB flows and to estimate

<sup>3</sup> We denote the actual density gradient by  $\alpha'$  in order to distinguish it from the initial gradient that is always denoted by  $\alpha$ .

also temporal variations of the last AGB mass-loss episodes by measuring expansion speeds of planetary nebulae, i.e. more precisely the flow velocities within the (outer) nebular shells of objects with a well developed double shell structure. These objects can be used as diagnostic tools to improve our knowledge concerning the mass-loss during the late AGB, i.e. from the last few 1000 up to about 50 000 years before the star left the AGB. In particular, we have found from the expansion rates of well known double-shell planetaries that in general this mass loss must increase towards the end of the AGB, leading to density stratifications in the AGB wind  $\rho \propto r^{-\alpha}$ , with  $2.5 \lesssim \alpha \lesssim 3.5$ , where  $\alpha$  increases with distance from the star.

Given existing mass-loss prescriptions which depend mainly on the stellar parameters luminosity, effective temperature and mass, the only way to obtain an  $\alpha$  increasing with distance from the star is a strong increase of the mass loss during the last few 10 000 years. This is possible during the star's recovery from the luminosity minimum after a thermal pulse, in conjunction with the rapidly decreasing stellar mass as a consequence of the mass loss. Indeed, the detailed hydrodynamical models computed by Steffen et al. (1998) led to circumstellar wind envelopes with slowly varying radial density gradients: from  $\alpha \lesssim 2$  close to the star to  $\alpha > 3$  further out (cf. also Steffen & Schönberner 2003, Figs. 1 and 2 therein).

In this context it is interesting to note a recent result reported by Kwok et al. (2002). They found from the radial  $21 \mu\text{m}$  intensity profile for the post-AGB object IRAS 07134+1005 that the radial density decline occurs with  $\alpha > 2.5$ .

Flatter halo density distributions with  $\alpha$  closer to 2 are possible if the star is in the advanced phase of its thermal-pulse cycle when the surface luminosity remains virtually constant. The majority of the PNe investigated in this study have expansion rates that are only explainable by rather steep radial density gradients of their circumstellar wind envelopes. Therefore, their central stars must have recovered from their last thermal pulse quite recently, and they are now in the hydrogen-burning stage of their post-AGB evolution, in agreement with what has been found in a study of a large sample of PNe with haloes (Corradi et al. 2003b). The mean kinematic age of these haloes is about 50 000 years, well below the thermal-pulse cycle time of about 100 000 years expected for core masses of about  $0.6 M_{\odot}$ .

The very fact that the mass-loss rate must stay at a level comparable to that typical for the tip of the AGB while the remnant is evolving off the AGB until effective temperatures around 6000 K are reached, cannot be accounted for by recent mass-loss formulas as those by Wachter et al. (2002) which are based on consistent modelling of dust formation and hydrodynamics. Because of their very strong dependence on the stellar temperature, these formulas would predict a decrease of the mass-loss rate by about 3 dex while the star is evolving from  $\approx 2500$  to  $\approx 6000$  K, which in turn would then increase the duration of this transit to several 10 000 years (cf. Schönberner & Blöcker 1993). Under these conditions of low circumstellar densities corresponding to mass-loss rates of  $10^{-6} M_{\odot} \text{ yr}^{-1}$  or less, the formation of a typical planetary nebula is not possible (Paper I). The bulk of the AGB matter expelled earlier when the rate was still very large is already at a distance of  $r \gtrsim 10^{17}$  cm

from the stellar surface when the remnant evolves into the PN domain.

Based on the insights of the present investigation, it is possible to construct an empirical density profile of the wind at the tip of the AGB such that the corresponding hydrodynamical PN model reproduces the observed relation between shell expansion velocity and stellar effective temperature shown in Fig. 12. The resulting empirical density profile can then be used to reconstruct the mass loss history during the evolution off the AGB. This novel idea will be pursued in future work.

A final remark concerns the concept of the “typical” expansion speed for planetary nebulae to be used e.g. in statistical studies. We have seen that the expansion rate of a PN shows a considerable evolution with time, and a value of  $20 \text{ km s}^{-1}$  which is often used in the literature as canonic value refers to the bright part, i.e. the rim, and is by no means an adequate value. High-resolution spectroscopy with large signal-to-noise ratios reveals the signature of the much faster expanding shells, with Doppler speeds of up to about  $40 \text{ km s}^{-1}$  (Fig. 12). In order to estimate the real expansion rate of a PN's outer edge, one has to multiply this Doppler speed by a factor of 1.3, as judged from our  $\alpha = 3$  models. This factor accounts for the difference between shock and postshock velocities ( $\approx 1.2$ ), and for the fact that the Doppler split monitors a region somewhat behind the shock where the flow velocity is lower (cf. Figs. A.1 and A.2).

Obviously PN expansion rates are larger than hitherto assumed, viz. up to about  $50 \text{ km s}^{-1}$ . Such high expansion rates last for a significant fraction of a PN's total lifetime and must be considered e.g. for any birth rate estimates in galactic contexts. We note here that all the expansion rates discussed in this paper are based on models with an elemental mixture considered to be typical for galactic disk objects. Planetary nebulae in metal-poor environments can cool less efficiently, and one expects substantially higher expansion rates of the shells since these scale with the sound velocity.

## Appendix A: Properties of models with power-law density distributions

In the following figures properties of model planetaries with power-law density distributions as initial configurations are illustrated at two selected positions,  $T_{\text{eff}} \approx 50\,000$  and  $\approx 100\,000$  K, along the horizontal part of the stellar evolutionary track. The structure of the models, as given by the densities and flow velocities, are shown together with the corresponding surface brightnesses in Figs. A.1 and A.2. Figure A.3 displays the profiles of the strongest [N II] and [O III] lines for the line-of-sight through the center of the models, computed with infinite spectral resolution. Due to the high density contrast between rim and shell the signatures of the shell's expansion are hardly seen in the figures for larger  $\alpha$ . For a further discussion, see Sect. 2.1.

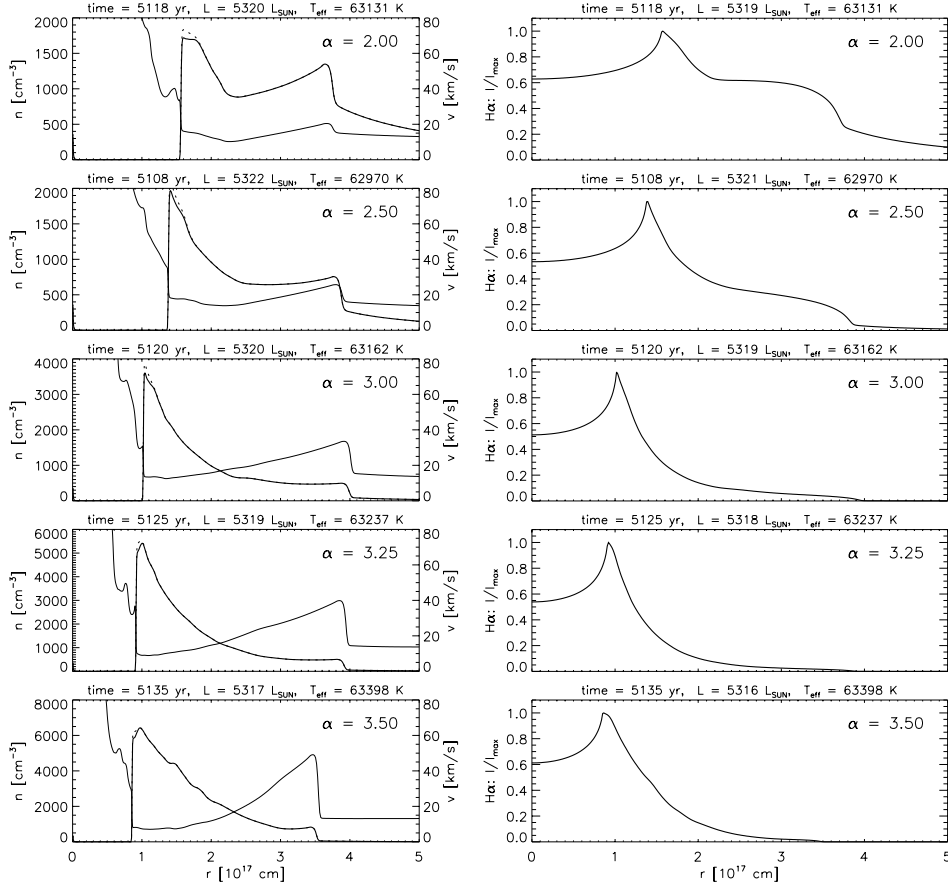


**Fig. A.1.** *Left:* Radial runs of heavy-particle number density (thick), electron number density (dotted), and flow velocity (thin) for various  $\alpha$  at a central star temperature of  $T_{\text{eff}} \approx 63\,500$  K, corresponding to  $t \approx 5150$  yrs for  $M = 0.595 M_{\odot}$ . *Right:* Radial distributions of the surface brightness in H $\alpha$ , normalized to maximum emission.

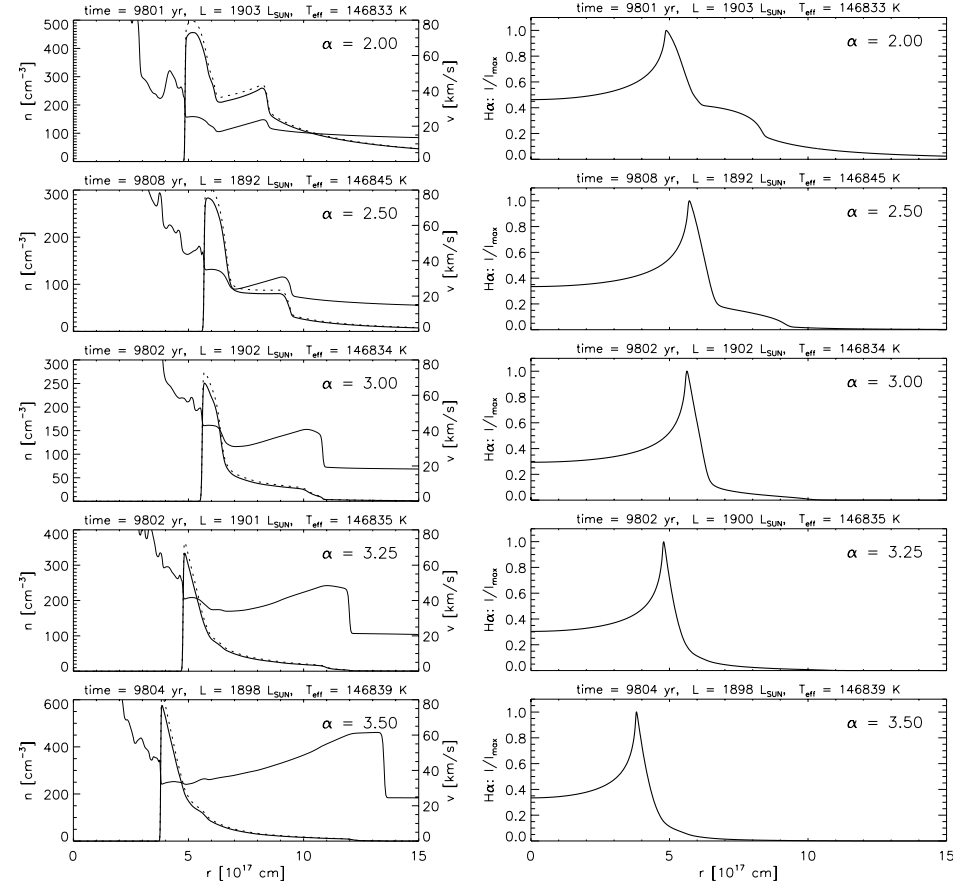


**Fig. A.2.** Same as in Fig. A.1, but close to the turn-around point,  $T_{\text{eff}} \approx 146\,800$  K and  $t \approx 9800$  years.

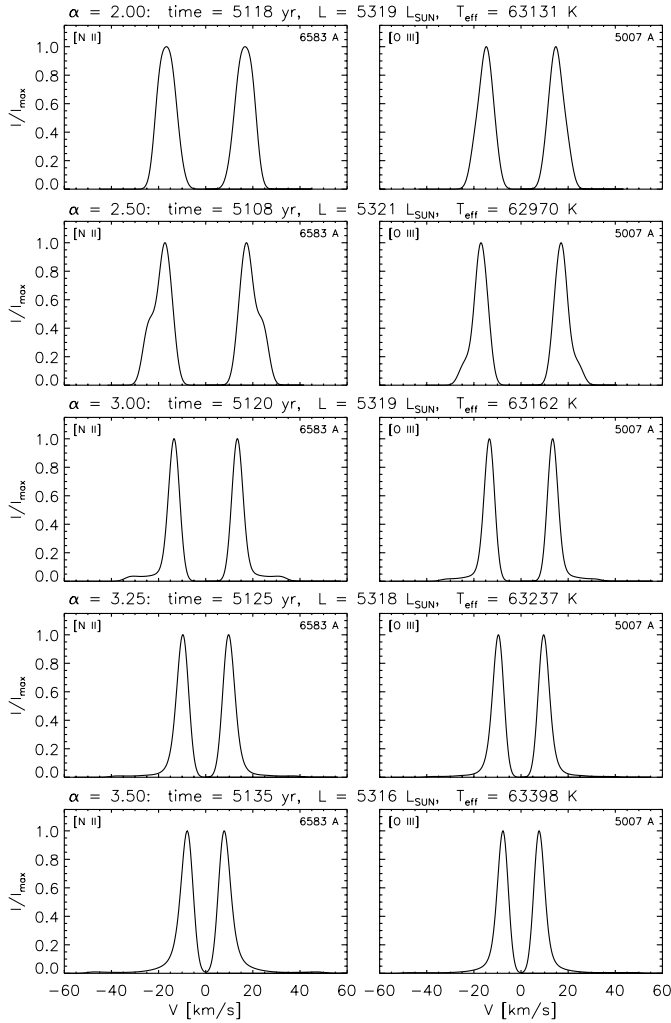


**Fig. A.3.** Emission-line profiles of [N II] 6583 Å (*left*) and [O III] 5007 Å (*right*) for the models shown in Fig. A.1. The profiles are computed along the central line-of-sight with a numerical aperture of  $1 \times 10^{16}$  cm radius and with infinite spectral resolution.

## References

- Alard, C., Blommaert, J. A. D. L., Cesarsky, C., et al. 2001, *ApJ*, 552, 289
- Chevalier, R. A. 1997, *ApJ*, 488, 263
- Chu, Y.-H., Kwitter, K. B., Kaler, J. B., & Jacoby, G. H. 1984, *PASP*, 96, 598
- Corradi, R. L. M., Schönberner, D., Steffen, M., & Perinotto, M. 2003a, in *Planetary Nebulae. Their Evolution and Role in the Universe*, ed. S. Kwok, M. Dopita, & R. Sutherland, IAU Symp., 209, 455
- Corradi, R. L. M., Schönberner, D., Steffen, M., & Perinotto, M. 2003b, *MNRAS*, 340, 417
- Franco, J., Tenorio-Tagle, G., & Bodenheimer, P. 1990, *ApJ*, 349, 126
- Gesicki, K., Acker, A., & Szczerba, R. 1996, *A&A*, 309, 907
- Gesicki, K., Acker, A., & Zijlstra, A. A. 2003, *A&A*, 400, 957
- Guerrero, M. A., Manchado, A., Stanghellini, L., & Herrero, A. 1996, *ApJ*, 464, 847
- Guerrero, M. A., Villaver, E., & Manchado, A. 1998, *ApJ*, 507, 889
- Hrivnak, B. J., Kwok, S., & Volk, K. M. 1989, *ApJ*, 346, 265
- Koo, B.-C., & McKee, C. F. 1992, *ApJ*, 388, 103
- Kwok, S., Volk, K., & Hrivnak, B. J. 2002, *ApJ*
- Marten, H., & Schönberner, D. 1991, *A&A*, 248, 590
- McCarthy, J. K., Méndez, R., & Kudritzki, R. P. 1997, in *Planetary Nebulae*, ed. H. J. Habing, & H. G. L. M. Lamers, IAU Symp., 180, 120
- Mellema, G. 1994, *A&A*, 290, 915
- Mellema, G. 2004, *A&A*, 416, 623
- Méndez, R. H., Kudritzki, R. P., & Herrero, A. 1992, *A&A*, 260, 329
- Neiner, C., Acker, A., Gesicki, K., & Szczerba, R. 2000, *A&A*, 358, 321
- Patriarchi, P., & Perinotto, M. 1991, *A&AS*, 91, 325
- Pauldrach, A., Puls, J., Kudritzki, R. P., Méndez, R. H., & Heap, S. H. 1988, *A&A*, 207, 123
- Perinotto, M., Schönberner, D., Steffen, M., & Calonaci, C. 2004, *A&A*, 414, 993 (Paper I)
- Plait, P., & Soker, N. 1990, *AJ*, 1883
- Reimers, D. 1975, in *Problems in Stellar Atmospheres and Envelopes*, ed. B. Baschek, W. H. Kegel, & G. Traving (Berlin: Springer), 229
- Sabbadin, F., Bianchini, A., & Hamzaoglu, E. 1984, *A&A*, 136, 193
- Sandin, C., & Höfner, S. 2003, *A&A*, 404, 789
- Schönberner, D., & Blöcker, T. 1993, in *Luminous High-Latitude Stars*, ed. D. D. Sasselov, ASP Conf. Ser., 45, 337
- Schönberner, D. 1990, in *From Miras to Planetary Nebulae: Which Path for Stellar Evolution?*, ed. M. O. Mennessier, & A. Omont (Éditions Frontières), 355
- Schönberner, D., & Steffen, M. 1999, in *Optical and Infrared Spectroscopy of Circumstellar Matter*, ed. E. W. Guenther, & S. Klose, ASP Conf. Ser., 188, 281
- Schönberner, D., Steffen, M., & Jacob, R. 2004, in *Asymmetric Planetary nebulae III*, ed. M. Meixner, J. Kastner, & N. Soker, ASP Conf. Ser., 313, 283
- Shu, F. H., Lizano, S., Galli, D., Cantó, J., & Laughlin, G. 2002, *ApJ*, 580, 969
- Steffen, M., & Schönberner, D. 2003, in *Planetary Nebulae. Their Evolution and Role in the Universe*, ed. S. Kwok, M. Dopita, & R. Sutherland, IAU Symp., 209, 439
- Steffen, M., Szczerba, R., & Schönberner, D. 1998, *A&A*, 337, 149
- Wachter, A., Schröder, K. P., Winters, J. M., Arndt, T. U., & Sedlmayr, E. 2002, *A&A*, 384, 452
- Weidemann, V. 2000, *A&A*, 363, 647
- Weinberger, R. 1989, *A&AS*, 78, 301